Clinical Cancer Research

Multispectral Optoacoustic Tomography (MSOT) of Human Breast Cancer

Gael Diot[1], Stephan Metz[2], Aurelia Noske[3], Evangelos Liapis[4], Barbara Schroeder[4], Saak V. Ovsepian[1,4], Reinhard Meier[2], Ernst Rummeny[2], and Vasilis Ntziachristos[1,4]

Abstract

Purpose: In a pilot study, we introduce fast handheld multispectral optoacoustic tomography (MSOT) of the breast at 28 wavelengths, aiming to identify high-resolution optoacoustic (photoacoustic) patterns of breast cancer and noncancerous breast tissue.

Experimental Design: We imaged 10 female patients ages 48–81 years with malignant nonspecific breast cancer or invasive lobular carcinoma. Three healthy volunteers ages 31–36 years were also imaged. Fast-MSOT was based on unique single-frame-per-pulse (SFPP) image acquisition employed to improve the accuracy of spectral differentiation over using a small number of wavelengths. Breast tissue was illuminated at the 700–970 nm spectral range over 0.56 seconds total scan time. MSOT data were guided by ultrasonography and X-ray mammography or MRI.

Results: The extended spectral range allowed the computation of oxygenated hemoglobin (HBO_2), deoxygenated hemoglobin (HB), total blood volume (TBV), lipid, and water contributions, allowing first insights into *in vivo* high-resolution breast tissue MSOT cancer patterns. TBV and Hb/HBO_2 images resolved marked differences between cancer and control tissue, manifested as a vessel-rich tumor periphery with highly heterogeneous spatial appearance compared with healthy tissue. We observe significant TBV variations between different tumors and between tumors over healthy tissues. Water and fat lipid layers appear disrupted in cancer versus healthy tissue; however, offer weaker contrast compared with TBV images.

Conclusions: In contrast to optical methods, MSOT resolves physiologic cancer features with high resolution and revealed patterns not offered by other radiologic modalities. The new features relate to personalized and precision medicine potential.
Clin Cancer Res; 23(22); 6912–22. ©2017 AACR.

Introduction

Despite advances in diagnosis and therapy, breast cancer remains a leading cause of mortality in women (1). Imaging plays a major role in breast cancer screening, early diagnosis, staging and monitoring the progression of the disease or treatment efficacy. X-ray mammography (XRM) is the most widely used modality for breast cancer detection, despite concerns over the use of ionizing radiation and reduced accuracy in dense breast tissue (2). Ultrasonography (US) is also used as a follow-up modality to differentiate nonmalignant cysts from other tumor types (3). Other methods, including MRI and nuclear imaging, have also been employed for breast cancer detection but are not widely employed due to increased cost and low throughput (4). Because of reliance on ionizing radiation, XRM and nuclear imaging methods are not appropriate for frequent imaging sessions, and hence, not suitable for longitudinal assessment of treatment effects. In addition to cost and low-throughput limitations, MRI may also require contrast agents for improving detection (5, 6), which complicate frequent use. Finally, US suffers from poor contrast and interoperator variability (7, 8). Therefore, despite a wealth of imaging approaches, there has been a constant search for imaging methods that offer complementary information and reduce possible health risks.

Optical imaging has been considered as an alternative to existing radiologic methods for breast imaging (9). Diffuse optical spectroscopy (DOS) and tomography (DOT) aimed to resolve pathologic alterations of breast tissue by recording oxygenated hemoglobin (HbO_2), deoxygenated hemoglobin (Hb), water, and lipids (10, 11). Hemoglobin images can enable assessment of two key cancer hallmarks: (i) angiogenesis, typically defined as total hemoglobin $Hb + HbO_2$ or total blood volume (TBV) content in tissue; and (ii) hypoxia, computed as the ratio of HBO_2 over TBV (12–15). Moreover, it has been recently observed that hemodynamic responses resolved by DOS can identify responders of neoadjuvant chemotherapy (16–19) within a day of treatment. These capacities, along with the low cost of optical instrumentation, the use of nonionizing energies and the ability to image through several centimeters (>5 cm) of breast tissue, make the optical method attractive for breast cancer imaging. Conversely, the low resolution achieved due to strong scattering compromises image fidelity and

[1]Chair of Biological Imaging, Technische Universität München, München, Germany. [2]Department of Radiology, Klinikum Rechts der Isar, Technische Universität München, München, Germany. [3]Institute of Pathology, Klinikum Rechts der Isar, Technische Universität München, München, Germany. [4]Institute of Biological and Medical Imaging, Helmholtz Zentrum München, Neuherberg, Germany.

Note: Supplementary data for this article are available at Clinical Cancer Research Online (http://clincancerres.aacrjournals.org/).

Corresponding Author: Vasilis Ntziachristos, Technische Universität München/Helmholtz Zentrum München, Ingolstädter Landstr., Neuherberg D-85764, Germany. Phone: 4989-3187-3852; Fax: 4989-3187-3017; E-mail: v.ntziachristos@tum.de

doi: 10.1158/1078-0432.CCR-16-3200

Translational Relevance

Multispectral optoacoustic tomography (MSOT) combines detection of optical contrast with resolution that is much higher than conventional optical imaging methods. In a pilot interrogation using handheld MSOT, we employed 28 wavelengths with frame rates of approximately 2 Hz to image 3 healthy volunteers and 10 breast cancer patients and identify MSOT imaging features of breast cancer. We show reconstructed images of total blood volume (TBV), oxygenated hemoglobin (HbO_2), deoxygenated hemoglobin (Hb), lipid, and water and observe vascularization and pathophysiologic changes in tumors versus healthy tissue. Initial results point to MSOT as a nonionizing, label-free method for imaging breast tissue with possible future applications to diagnostics and the assessment of treatment response.

quantification and has restricted the widespread clinical application of optical imaging methods.

Optoacoustic imaging is a hybrid imaging modality that resolves optical absorption with resolution that is significantly improved over optical imaging. Resolution improvements lead to better image fidelity and accuracy (20–22). The technique has been considered for breast cancer imaging since the late 1990s (23–25), using different implementations and imaging geometry designs. One design trend has been the use of rigid imaging chambers to contain the target tissue and position the optical illumination and ultrasound components at predetermined positions in relation to the object scanned (23, 24, 26–31). Typically, the patient lies in the prone position on a bed with the rigid imaging chamber. Alternatively, handheld optoacoustic imaging has been considered for breast cancer imaging, using a linear ultrasound array retrofitted with an illumination source for optoacoustic signal generation (32). Notably, optoacoustic imaging of the breast has used at most two wavelengths, which affords limited information on the spectral content of the breast tissues (28, 32, 33). While rigid imaging chambers may allow three-dimensional data collection and reconstruction, handheld scanners are more versatile in their use and can operate similarly or simultaneously with US, also applied in handheld mode (32).

We have recently developed a new class of lasers and handheld optoacoustic systems that can perform fast wavelength scanning (20, 34). Up to 100 different wavelengths can be scanned each second. Moreover, fast data acquisition hardware can acquire up to 512 channels in parallel, enabling real-time image acquisition. The rich availability of wavelengths can enhance the readings of the optoacoustic method (35). In particular, it has been recently shown that increasing the number of wavelengths, over previous implementations using two wavelengths, can lead to marked improvements in spectral unmixing accuracy and sensitivity (36). Taking advantage of these developments, we introduce handheld MSOT based on fast-tuning pulsed lasers for multispectral imaging of healthy human breast and breast cancer. In a pilot study using 28 wavelengths ranging between 700 and 970 nm and 50-Hz pulsing rates, we resolve the distribution of hemoglobin, lipid, and water in human volunteers and patients. The primary goal of the study was to identify the patterns achieved by breast MSOT due to the high resolution offered and interrogate possible differences between malignant tumors and between malignant tumors and nonmalignant breast tissue. We identify a characteristic disruption of Hb and HbO_2 signals, leading to marked TBV pattern differences between healthy and cancerous breast tissue. We further identify spatial heterogeneity differences between tumors in different patients. We discuss the implications of the findings in terms of designing phase II clinical trials based on handheld breast cancer MSOT.

Materials and Methods

Handheld MSOT

The custom-built handheld MSOT scanner has been described previously (34). In brief, illumination is provided by a tunable pulsed laser (Spitlight 600 DPSS, Innolas Laser) with a working range of 680–980 nm on a per-pulse basis and a repetition rate of 50 Hz. Pulse length was 8 ns, and maximum energy at 700 nm was approximately 15 mJ. A custom-made fiber bundle (CeramOptec Germany) delivered light in a line configuration (40×1 mm^2). Optoacoustic signals were detected using a 256-element piezoelectric transducer array in which the elements were arranged in a half arc spanning 174°. The array diameter was 120 mm, and the central frequency was 5 MHz (see ref. 34 for a detailed description). The transducer was enclosed in an optically and acoustically transparent low-density polyethylene membrane, with the cavity between the half-arc detector and specimen filled with heavy water (D_2O) for optimal acoustic coupling. The 220-mL D_2O cavity does not come into contact with the patient and requires topping-up (5–10 mL) every few months. A custom-built analog-to-digital 256-channel converter was used for parallel data acquisition at a sampling rate of 40 MS/second and 12-bit digital resolution. To enable real-time viewing of the acquired images, a delay and sum image reconstruction algorithm was implemented on a graphics-processing unit (GPU) that rendered frames at 50 Hz in a graphical interface.

Patients

Ten patients ages 48–81 years that had been diagnosed with malignant, nonspecific breast cancer ($n = 8$) or invasive lobular carcinoma ($n = 2$) at the Klinikum Rechts der Isar of the Technische Universität München (Munich, Germany) were examined using handheld MSOT. Three of the patients were premenopausal, while the remaining 7 were menopausal or postmenopausal. All patients were diagnosed initially based on lesions observed by XRM, US, and/or MRI, and the diagnosis was confirmed on the basis of core-needle biopsy. Tumors, which ranged in size from 5 to 50 mm in the long dimension, were classified by an expert radiologist based on the Breast Imaging Reporting and Data System classification scale and IHC (HER2, ER, and PR; ref. 37). All participants gave written informed consent to participate in the study, which was approved by the Government of Upper Bavaria and by the Ethics Review Board of the Klinikum Rechts der Isar (Munich, Germany).

Imaging protocol

All patients and healthy controls were scanned by US and MSOT in the supine position. In patients, the masses seen by XRM were located using US (Logiq E9, GE Healthcare), and then the same tissue area was scanned using handheld MSOT

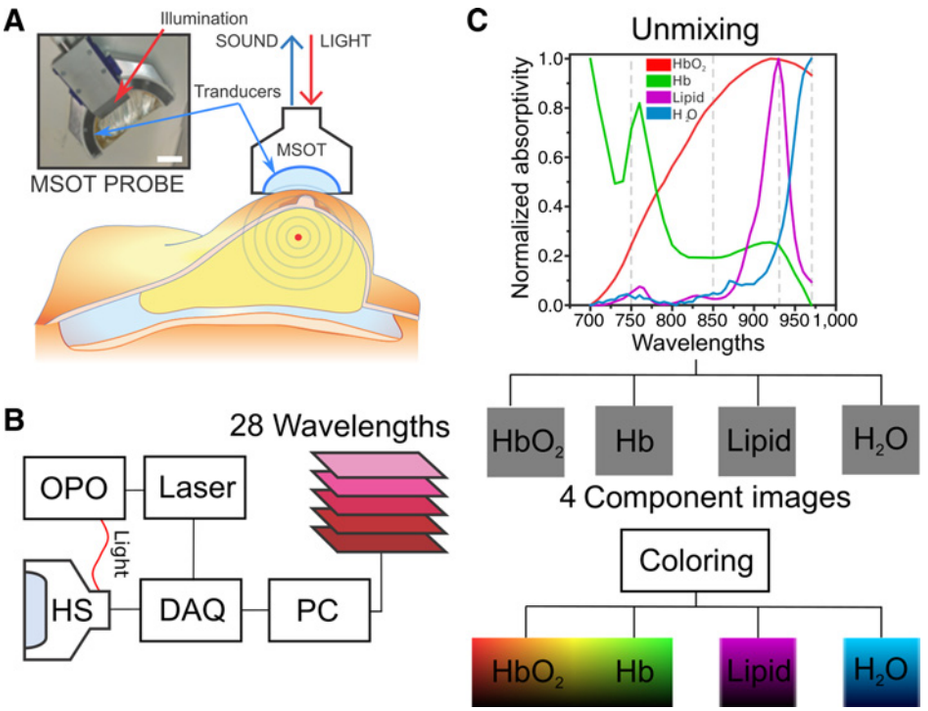

Figure 1.

A, Photograph of the handheld MSOT probe and a schematic of MSOT scanning breast tissue. **B,** Hardware components employed in image acquisition and generation of a multispectral dataset at 28 wavelengths. HS, handheld scanner; DAQ, data acquisition unit; OPO, optical parametric oscillator; PC, personal computer. **C,** Normalized absorptivity graph of four key absorbers in the breast tissue in the range of wavelengths used. On the basis of defined spectra, distributions of the four different components (HbO_2, Hb, lipid, and water) were extracted from the 28 acquired frames and assigned a different color.

(Fig. 1A), during which slight pressure was applied to reduce the tumor's depth. A real-time reconstruction algorithm was used to display the resulting images on a graphical user interface (GUI), with raw data stored in parallel for offline post-processing and data analysis. For each MSOT position scanned (cross-sectional slice), 28 frames were collected at wavelengths from 700 to 970 nm in 10-nm steps. Each multiwavelength slice of 28 frames took approximately 0.56 seconds to acquire (i.e., 50-Hz laser pulse repetition rate with a different wavelength for each pulse). The laser pulses triggered the data acquisition (DAQ) module (Fig. 1B). We did not employ data averaging, to minimize motion artifacts. Therefore, each single image collected was acquired with a single pulse illumination. Total examination time was 2–4 minutes.

Data analysis and image representation

Data was processed offline with MATLAB R2014b (Mathworks). First, a Butterworth bandpass filter was applied with cut-off frequencies 0.25 MHz and 10 MHz, and signals were corrected for laser energy fluctuations, using an internal photosensor that is recording laser output. The sensor was integrated into the laser module, and images obtained at different wavelengths were reconstructed on the basis of a model-based reconstruction algorithm (38). Subsequently, the reconstructed images were linearly unmixed, using the spectra of the four main endogenous absorbers in the 700–970 nm range (Fig. 1C), that is, oxygenated hemoglobin (HbO_2), deoxygenated hemoglobin (Hb), lipid, and water (H_2O), in the 700 to 970 nm spectral range (39). This resulted in four separate images, each corresponding to one of the main absorbers (Fig. 1C). Different colormaps were selected to represent the distributions of the four absorbers: HbO_2, red; Hb, green; lipid, magenta; and H_2O, blue. Image processing calculating image metrics, including average values over regions of interest and image profiles employed for assessing spatial heterogeneity, were performed on MATLAB (Mathworks). Total blood volume (TBV = Hb + HbO_2) ratios were calculated for 5 × 5 mm^2 regions of interest from high TBV values on the tumor rim to background tissue, that is, normal breast tissue away from the tumor. Spatial TBV gradients through tumors were calculated by fitting a line (radius) of 5-mm length to the intensity values across a TBV profile from the center of the tumor to the outer boundary of the tumor and plotting the resulting slope. Similar 5-mm profiles were also drawn in adjacent healthy tissue to obtain reference spatial gradient measurements.

Results

Figure 2 shows MSOT measurements from a healthy volunteer. Images acquired at different wavelengths reveal different structural information and contrast (Fig. 2A–D). Images at wavelengths in the 700–850 nm range depict a layer of strong signal from the tissue surface (i.e., skin), with an underlying layer of weak optoacoustic signal and then, at lower depth, an area containing several high-resolution structural features attributed to vascular structures. Images at shorter wavelengths (i.e. 750, 850 nm; Fig. 2A and B) showed higher resolution and contrast compared with images at longer wavelengths (i.e. 930 nm; Fig. 2C) reflecting the fact that longer wavelengths are representative of fat and water signals, which reduces contrast in observing hemoglobin. This is in particular evident at >930 nm images (i.e. 970 nm; Fig. 2D), which exhibited a low-spatial variation pattern due to the fact that lipids and water are broadly distributed throughout the breast. Spectral unmixing applied to all 28 wavelengths produced a set of four images, that is, HbO_2, Hb, lipid, and water (Fig. 2E, G, H). Figure 2F shows an image of total blood volume,

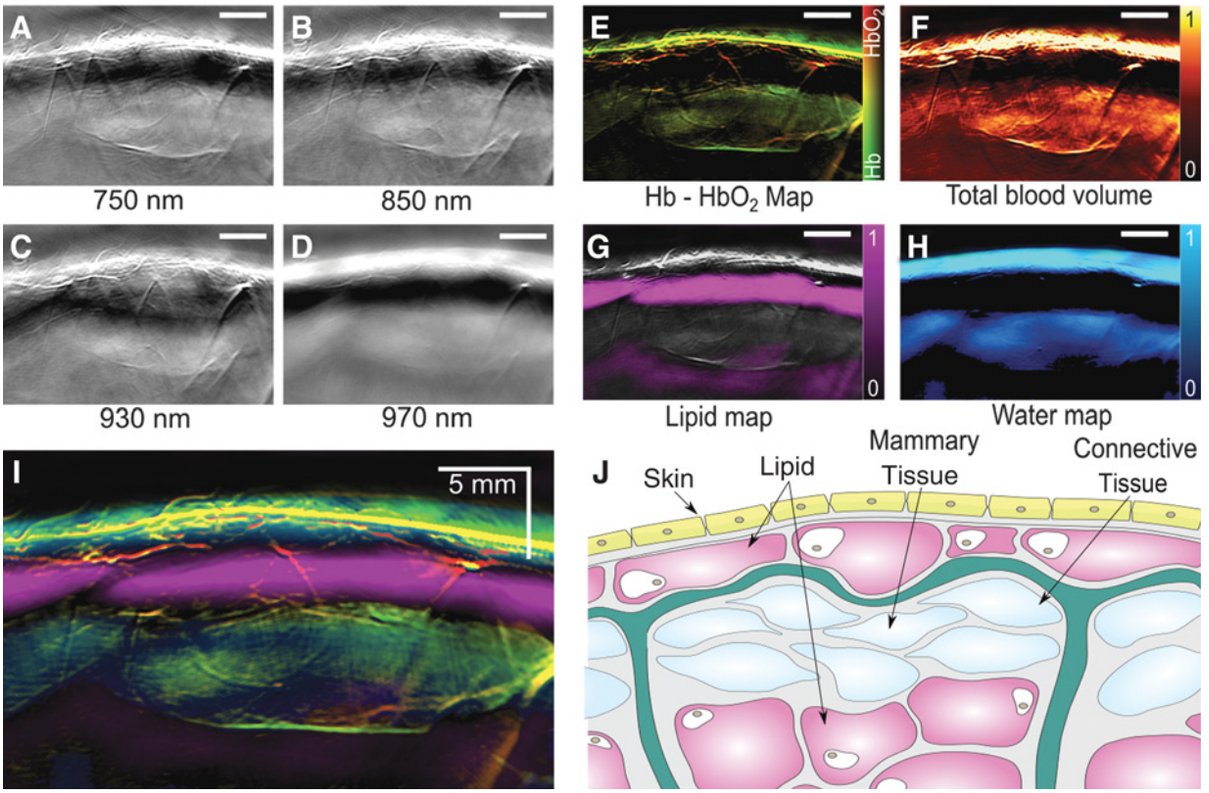

Figure 2.

MSOT images of healthy breast tissue revealing spectral and structural information from four endogenous absorbers. **A–D,** Raw images acquired at four different wavelengths. **E,** Image of HbO_2 and Hb distribution after unmixing of the raw images (**A–D**). **F,** Image of total blood volume distribution. **G** and **H,** Lipid and water components after unmixing as in **E** and **F**. **I,** Composite image of all four absorbers, revealing the layered structure of the breast. **J,** Schematic of the structure and layers of the human breast: yellow, skin; pink, lipid; light blue, mammary tissue; green, connective tissue known as Cooper ligament. Scale bars, 5 mm.

calculated as the sum of HbO_2 and Hb components. A composite image showing the overlap of all four components is depicted in Fig. 2I.

Clearly distinguishable features are present in the different tissue components, pinpointing a stratified organization of the breast tissue, with HbO_2 and Hb revealing vascular-rich tissue areas and vessels (Fig. 2E, F, I), supplying the dermal layer and mammary tissue, whereas the subcutaneous fat and retro-mammary adipose tissue receive sparser vascularization. Anatomically, the information provided by the four components resolved (Fig. 2E–I) is in agreement with the stratified anatomy of the healthy breast (Fig. 2J). The dark subcutaneous layer in Fig. 2A, B, and D, more clearly resolved in Fig. 2G, likely represents a fat layer because it showed stronger optoacoustic signal at 930 nm (Fig. 2C), near the peak absorption for lipids (Fig. 1C). Future work is needed to verify whether this dark layer corresponds to lipids or to wave reflections or other effects.

Next, we used handheld MSOT to image breast cancer. Fig. 3 presents two cases of a 5-mm diameter nonspecific carcinoma and a 15 × 20-mm diameter invasive lobular carcinoma. The 5-mm tumor was a superficial mass with a center at a depth of approximately 8 mm. The tumor was imaged by MRI after gadolinium injection (Fig. 3A and B) and was visible both by US (Fig. 3C) and MSOT (Fig. 3D). Contrast enhancement with gadolinium shows a "rim enhancement" effect, corresponding to a tumor that is peripherally perfused but with a core of reduced blood perfusion (Fig. 3B). MSOT resolves a similar pattern of rim enhancement indicative of strong peripheral vascularization and a core of low optoacoustic signal, observed in Hb–HbO_2 images (Fig. 3E) and TBV (i.e. Hb + HbO_2) images (Fig. 3F). Slight but clearly discernible distortion of the lipid and water layers is also evident in the healthy tissue surrounding the breast, possibly due to invasion of the tumor into the adipose tissue and an overall disruption of healthy tissue structures (Fig. 3G and H). Postoperative histology of breast tissue stained with anti-CD31 antibody confirmed the rim enhancement of vascularization (arrows, Fig. 3I), and staining with hematoxylin–eosin identified a dense tumor core (arrow, Fig. 3J).

Figure 3K–Q depict the case of the larger tumor (15 × 20 mm), pathologically characterized as invasive lobular carcinoma approximately 17 mm under the skin surface. The breast of this patient was denser, as reflected in the high XRM signal from the tissue surrounding the tumor (Fig. 3K), while the tumor itself was clearly visible as a large area of high density (arrow). US also resolved a large solid mass with hypoechoic appearance and ill-defined margins (Fig. 3L), measuring 15 mm along the short and >20 mm along the long dimension. MSOT clearly detected a disruption of the layered structure seen in healthy adipose and

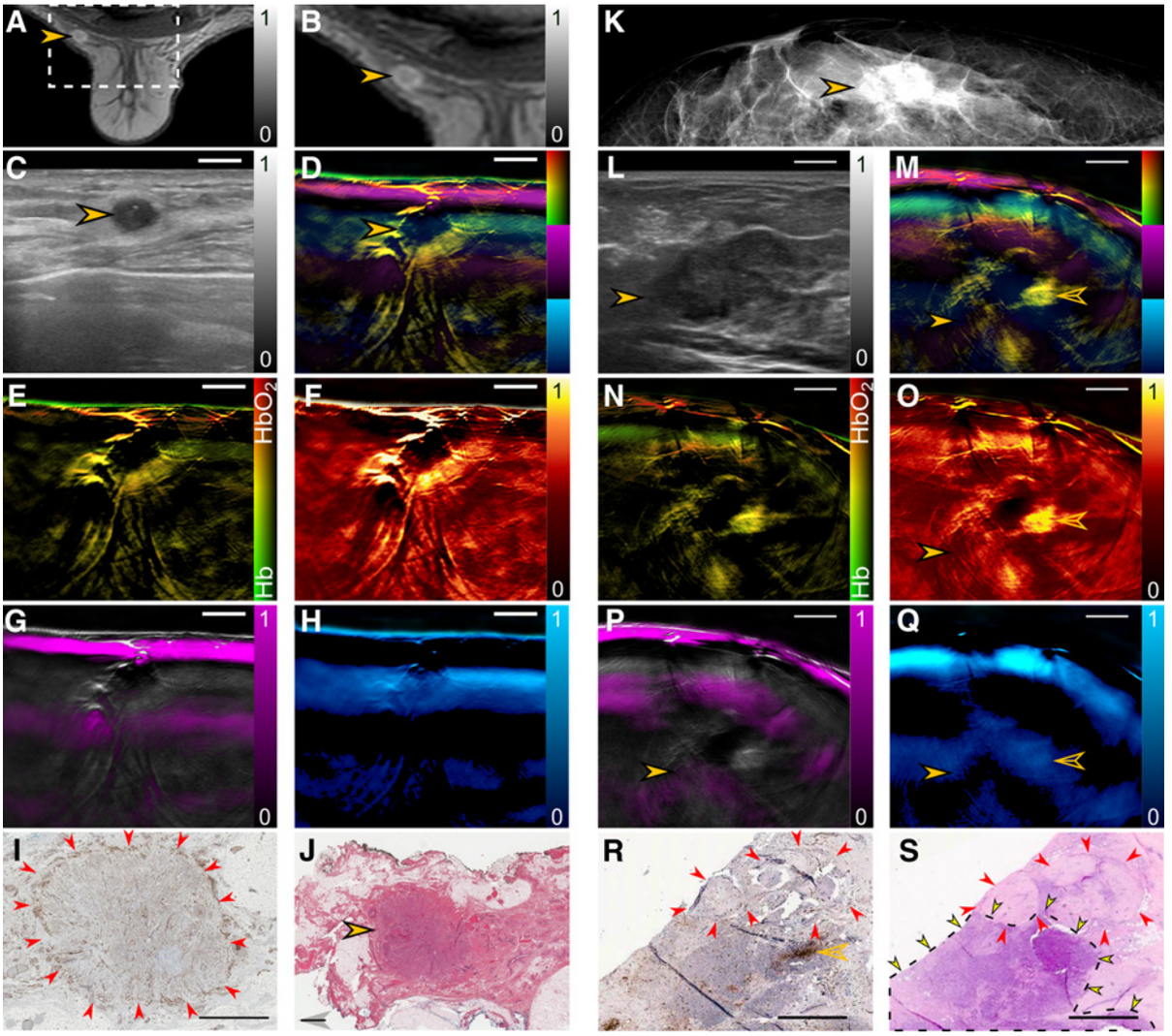

Figure 3.

Multimodal imaging of nonspecific cancer and invasive lobular carcinoma. **A,** Axial postgadolinium MRI showing a 5-mm diameter nonspecific breast tumor located at approximately 8-mm depth. The tumor location is indicated with an orange arrow. **B,** Enlarged image of the boxed area in **A**. The arrow indicates the tumor body. Higher gadolinium intake (contrast) is visible on the periphery of the tumor, while the tumor core appears darker, suggestive of reduced perfusion. **C,** US image of the same tumor providing complementary structural information. **D,** Composite MSOT image of the same tumor showing all four key absorbers after unmixing. **E,** MSOT image color-coding the distributions of Hb and HbO_2. **F,** MSOT image of total blood volume (TBV). **G,** MSOT image of fat content. **H,** MSOT image of water content. **I,** Anti-CD31 IHC staining of a cross-sectional slice through the tumor obtained postoperatively. **J,** H&E staining of a slice adjacent to the one in **I**. Scale bars (**A–H**), 5 mm. Scale bars (**I** and **J**), 2 mm. **K,** XRM image from a second patient shown a 15 mm × 20 mm invasive lobular breast carcinoma indicated by a solid orange arrow. **I,** US image revealing a center at location of approximately 17-mm deep. **M,** Composite MSOT image, indicating a strong disruption of the layered structure of the tissue around the tumor. **N,** MSOT image of hemoglobin (Hb and HbO_2) map. **O,** MSOT image of total blood volume. **P,** MSOT image of lipid. **Q,** MSOT image of water. **R,** Anti-CD31 IHC staining of a cross-sectional slice through the tumor obtained postoperatively. **S,** H&E staining of a slice adjacent to the one in **R**. Scale bars (**K–Q**), 5 mm. Scale bars (**R** and **S**), 2 mm.

fibroglandular tissue. Figure 3M–Q show MSOT images, which revealed disruption of the normal layered structure of adipose and fibroglandular tissue. Part of the tumor appeared as a dark area (solid arrow) surrounded by areas of increased but irregular vascularization inside the tumor (TBV), with patches of increased hemoglobin signals (Fig. 3M, N, and O, hollow arrow), with only one region of the tumor appearing avascular. The avascular tumor region measured approximately 3 mm, smaller than the tumor's diameter of 15 by 20 mm. No lipid signal was detected inside the tumor (Fig. 3P), while patchy water signals were observed in and around the tumor (Fig. 3q). Postoperative histology of breast tissue stained with anti-CD31 antibody confirmed the presence of a highly vascularized area (Fig. 3R, hollow arrow), next to an avascular region (red arrows). Hematoxylin and eosin (H&E) staining (Fig. 3S) revealed that the avascular area corresponded to a fibroadenoma (red arrows), next to

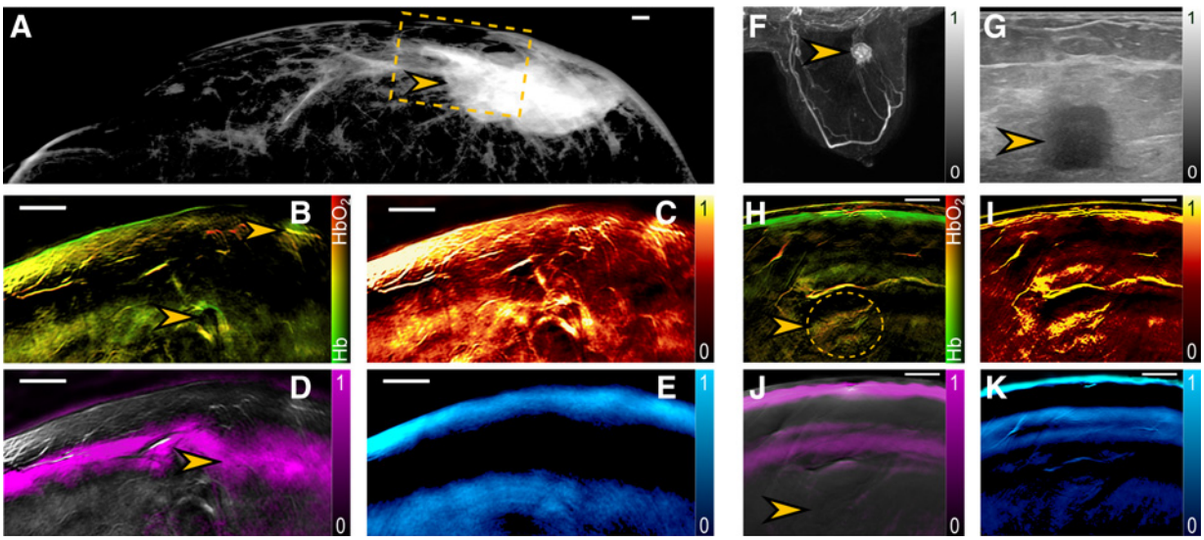

Figure 4.

Multimodal imaging of the largest and the deepest seated tumor in the study. **A,** XRM image revealing a >4 cm, subcutaneous, nonspecific breast tumor by XRM and MSOT. The field of view imaged by MSOT is approximately indicated by a dashed line box. **B,** MSOT image of Hb and HbO_2 obtained from the box in **A**; arrows point to areas of increased blood volume. **C,** MSOT image of TBV showing constitutive hyperemia through an extended area of the tumor. **D,** MSOT image of lipid showing disruption of the fat layer (arrow) at the area of the tumor mass. **E,** MSOT image of water. **F,** Axial MRI breast image after gadolinium injection from a second patient with a triple negative approximately 12-mm diameter nonspecific tumor. **G,** US image of the same tumor resolving the tumor at a depth of approximately 22 mm. **H,** Hb, HBO_2 MSOT map. **I,** TBV revealing patches of increased intensity surrounding the tumor. A large blood vessel appears to infiltrate the tumor. As in previous cases, the core of the tumor appears avascular. Lipid map (**J**) and H_2O map (**K**) showing disruptions in the tumor area. Scale bars on MSOT images, 5 mm.

mammary carcinoma (dotted line + yellow arrows). MSOT allowed in this case differentiation of two types of tumors through their vascularization pattern. The complementarity of contrast between ultrasonography and MSOT is also evident in the images, with US imaging capturing the extent of the entire lesion, whereas MSOT only resolving vascularization associated with the malignant part of the tumor.

Figure 4 shows two additional cases from the largest tumor imaged and deepest seated tumor imaged. Figure 4A shows a nonspecific breast carcinoma imaged by XRM and measuring >4 cm in the longer diameter. The tumor and surrounding vasculature virtually occupied the entire MSOT field of view (Fig. 4B–E). The MSOT images demonstrate highly irregular disruption of the layered tissue seen in healthy tissue (Fig. 2). MSOT images showing Hb/HbO_2 (Fig. 4B) and total blood volume (Fig. 4C) revealed irregularities of vascularization and blood distribution, with patches of high HbO_2 throughout the tumor. Superficial and deeper areas of the tissue show patches of increased blood volume, many with high levels of Hb (Fig. 4B). Disruptions of the layered tissue structure were also evident from the spectral maps of lipid (Fig. 4D), which revealed a diffusive signal region (arrow) that may be due to the invading tumor mass. The water signal does not show clear evidence of disruption (Fig. 4E).

A triple negative nonspecific carcinoma was imaged at depth of approximately 2.2 cm (tumor extended at depths from ~ 1.7–3 cm) Postgadolinium MRI (Fig. 4F) revealed a circular tumor measuring approximately 12 mm in diameter, also seen on ultrasound images as a hypoechoic lesion (Fig. 4G). MSOT images (Fig. 4H–K) show a lesion of increased vascularization with patchy appearance and, as in the previous cases an avascular center appearing dark on the Hb, HbO_2 (Fig. 4H) and TBV images (Fig. 4I). A large feeding vessel appears entering the tumor on the top side of the image (Fig. 4H and I). No significant disruption is seen on the lipid layers (Fig. 4J) and a minor water disruption is seen on the water image (Fig. 4K).

Figure 5 shows measurements from two additional breast cancer patients and compares images obtained from adjacent planes in the tumor. Figure 5A presents XRM imaging with iodine-enhanced contrast of a dense breast with a tumor of diameter approximately 20 mm lying at a depth of 5 mm. The US image of the same area displays a hypoechoic tumor with a highly irregular boundary (Fig. 5B). The corresponding MSOT image (Fig. 5C and E) clearly resolves a tumor mass, exhibiting a patchy rim enhancement indicative of increased blood volume areas. Moreover, a large vessel measuring approximately 2 mm in diameter seems to reach into the tumor center. Layer disruptions are seen both in the fat and water images. An adjacent MSOT image, obtained approximately 5 mm apart from image (Fig. 5E), exhibits a different appearance as it resolves a different part of the tumor mass. A patchy enhancement of TBV is observed (Fig. 5D and F), but no central dark area is visible. A layer disruption is seen on both the fat (Fig. 5H) and water layers (Fig. 5J). Images from another patient (Fig. 5K–T) show a breast tumor measuring 25–30 mm in the longer diameter in a second patient. Adjacent MSOT planes 5-mm apart are rendered again to examine differences through different slices through the tumor. Figure 5K shows the XRM of the breast tumor measuring 25–30 mm in the longer diameter. Irregular, spiculated borders are clearly

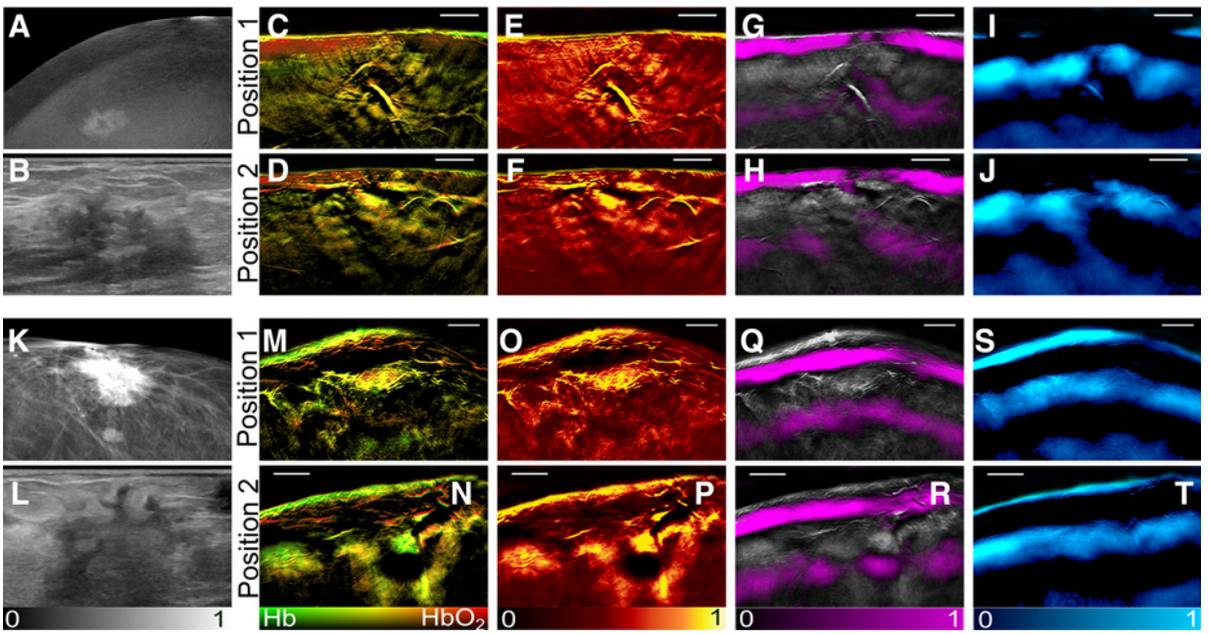

Figure 5.

Individualized tumor heterogeneity revealed by MSOT analyzed in two additional patients. **A,** Iodine-enhanced XRM of a breast tumor showing a nonspecific carcinoma measuring 13 mm in diameter. **B,** US image of the same tumor. **C,** Cross-sectional Hb–HbO_2 image through the tumor. **D,** An adjacent cross-sectional Hb–HbO_2 image through the tumor, obtained 5-mm apart from the section in **C**, exhibiting a different pattern of angiogenesis. **E** and **F,** TBV maps corresponding to **C** and **D**. **E** depicts a large vessel entering the core of the tumor and an overall reduced TBV value at the tumor core. **G** and **H,** Corresponding lipid cross-sections showing disruption of the retro-mammary layer with lipid invasion into the tumor core. **I** and **J,** MSOT cross-sectional images of the water component showing local disruption of the water content. **K** and **L,** XRM and US images of an irregularly shaped tumor with diameter 2.5–3 cm. **M** and **N,** Adjacent Hb–HbO_2 maps 5-mm apart showing high density of small vessels at the edges of the tumor. **O** and **P,** Corresponding TBV images exhibiting differences of angiogenesis patterns through the tumor. Lipid maps (**Q** and **R**) and H_2O maps (**S** and **T**) showing disruption of the lipid layer and reduced H_2O in the tumor-affected area.

discernible on the US image (Fig. 5I). MSOT resolves rim enhancement in the TBV image, surrounding a dark mass (Fig. 5M and O). Figure 5Q shows the lipid layer, revealing minor disruption, while Fig. 5S shows the water layer, which indicated no apparent tumor-induced changes. In the second imaging plane (Fig. 5N and P), Hb/HbO_2 and TBV MSOT images revealed features different from those in the first imaging plane, including different patches of high Hb signal as well as strong HbO_2 signal around a dark avascular core. This suggests increased angiogenesis of areas surrounding an apparent weaker signal mass lying deeper than in the first imaging plane (arrow). US confirmed hypoechoic areas that extended deeper than the main mass (arrow on Fig. 5L), which is clearly seen on the MSOT images (Fig. 5N, arrow). This secondary dark-center mass (Fig. 5N and P, arrow) shows rich lipid content (Fig. 5R), which was unusual among the lesions analyzed in this study. Overall, this secondary lesion also appears to impart a disruption of the deeper fat layer (Fig. 5R), but not prominently in the water layer (Fig. 5T).

To better understand the manifestation of the MSOT features resolved in breast cancer, we computed two parameters based on the imaging feature observed, that is, the TBV tumor-to-background ratio (Fig. 6A) and the TBV gradient (Fig. 6B). The first parameter computed the ratio of the TBV (TBV = Hb + HbO_2) seen in highly vascular areas of tumors versus background normal tissue over a 5×5 mm^2 ROI. The TBV ratio indicates the relative angiogenesis in tumors and reached values as high as 30-fold (Fig. 6A). The ratio in tumor #3 is computed for the patient shown on Fig. 4A–E. Because of the large area occupied by the tumor, it is not likely in this case that normal tissue is present on the image; therefore, the value may not represent an accurate tumor-to-background ratio. The findings demonstrate that in all cases, there is a marked increase in TBV signal in cancerous tumors, indicative of angiogenesis. Nevertheless, the findings also demonstrated significant variability between tumors, allowing observations on the individual tumor level. Because of the presence of high resolution images, intratumoral variability could also been observed. To capture aspects of tumor heterogeneity we also applied the TBV gradient as a metric of tumor spatial heterogeneity. The TBV gradient (Fig. 6B) was calculated as the angle of a 5-mm line profile (radius) applied to tumors and adjacent noncancerous tissue. The TBV gradient indicates spatial heterogeneity from the periphery to the center of the tumor and similarly exhibited more than 5-fold variability for different tumors imaged. The strongest gradient value is in the case of patient #4, which was a triple-negative stage 3 tumor, followed closely by patient #7, which was a double negative (PR^-, $HER2^-$) patient. Figure 6C shows a summary of the IHC readings for estrogen receptor (ER), progesterone receptor (PR), and tyrosine–protein kinase receptor (HER 2) for all patients. The age, sex, and tumor grading and type are also specified.

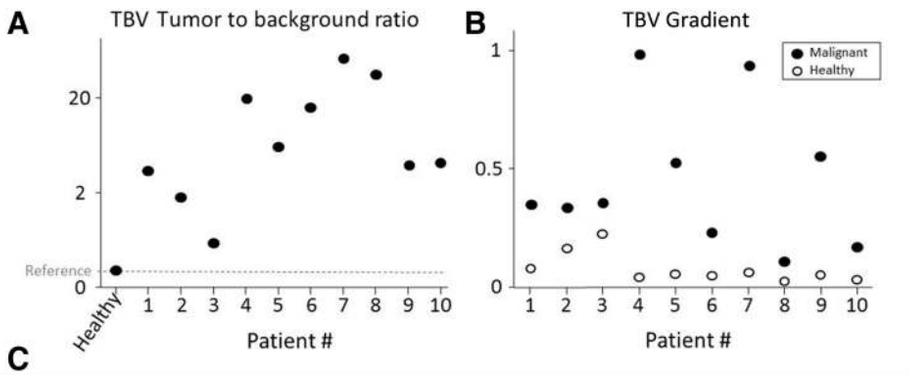

C

	Sex	Age	Type	Stage	ER	PR	HER 2
Patient 1	F	74	NST	2	pos	pos	pos
Patient 2	F	64	ILC	2	pos	pos	neg
Patient 3	F	81	NST	2	pos	pos	neg
Patient 4	F	57	NST	3	neg	neg	neg
Patient 5	F	81	NST	2	pos	pos	neg
Patient 6	F	82	NST	2	pos	pos	2+
Patient 7	F	76	NST	2	pos	neg	neg
Patient 8	F	61	NST	2	pos	pos	neg
Patient 9	F	48	ILC	2	pos	pos	neg
Patient 10	M	73	NST	2	pos	pos	2+

Figure 6.
Quantification of tumor parameters compared with healthy tissue. **A,** Ratio of the TBV intensity in tumors compared with healthy tissue. Healthy tissue is set as the reference at value 1. We note that the TBV ratio calculation for patient #3 may not be representative of true tumor-to-background ratio as the tumor was very extended spatially (see Fig. 3) and the entire field of view of the MSOT image may have not contained truly healthy tissue. **B,** Intensity gradient across tumor compared with healthy tissue. **C,** Table containing the IHC (ER–PR–HER 2) results, the age, the type of tumor, and the stage of all the scanned patients.

Discussion

We performed a pilot imaging study aimed to identify MSOT patterns in healthy breast tissue and breast cancer, resolved in label-free mode. Handheld MSOT is emerging in clinical applications; however, it has never been previously applied to breast cancer studies. Observation of breast MSOT patterns revealed recurring features including high peripheral vascularization, increased TBV heterogeneity over normal tissue, low intratumoral vascularity, disruption of tissue layers such as fat and water layers, and patchy appearance of Hb and HBO_2 signals.

High-peripheral vascularity was visualized on Hb, HbO_2, and TBV images, which demonstrated areas of increased TBV indicative of angiogenesis, a hallmark of cancer development (40–43). Compared with healthy breast tissue, tumor areas exhibited a strong heterogeneous TBV pattern with markedly reduced vascularization in the tumor core. High-resolution MSOT patterns of angiogenesis and tumor vascular heterogeneity were captured by the TBV ratio and the TBV gradient calculations, respectively (Fig. 6). Regions of interest from the tumor periphery (rim) versus adjacent noncancerous tissue demonstrated target-to-background Ratios (TBR) that could reach values of >30-fold increase (Tumor #7, #8; Fig. 6A).

CD31 IHC analysis on surgically excised specimen (e.g., Fig. 3I and R) confirmed patches of high vasculature surrounding the tumor. The reduced optoacoustic signal (dark area) observed in the core of tumors is explained herein as low intratumoral vascularization. Histopathology analysis of the tumor core, available for a subset of tumors that did not receive neoadjuvant chemotherapy (Fig. 3I and J) revealed vessels with size that would generate high ultrasound frequencies (>7 Mhz), which are not detected by the ultrasound transducer employed. It is unlikely that this lack of signal is due to light blockage because of increased photon absorption by the increased vascularization, as there are no "shadowing" effects observed by the tumor. Moreover, Fig. 5A clearly resolves a large blood vessel reaching the tumor center, corroborating the hypothesis that light reaches the tumor core. Tumors also exhibited marked spatial heterogeneity of vascular features, with normalized gradient differences ranging from 0.2 to 1 (Fig. 6B) and the TBV gradient assuming the highest values for the two PR-negative patients in the study (patient #4, #7).

MSOT also allowed the observation of the individual HbO_2 and Hb images contributing to TBV and consistently demonstrated patches of increased HbO_2 content in the tumor periphery. Some tumors were shown to contain strong deoxygenated hemoglobin signals, indicative of settling hypoxia into the tumor mass. However, this observation was not present in all tumors, possibly pointing to a variation in hypoxia between tumors. MSOT also resolved an apparent disruption of the lipid and water layered structures observed in healthy breast. The disruption was seen on all images; however, its strength varied significantly and did not preliminary evince on an MSOT pattern with diagnostic potential, as not all tumors could be clearly identified on the fat or water images. Imaging of large tumors in Fig. 4 and Fig. 5Q showed strong lipid infiltration in the tumor area, whereby imaging of smaller tumors, such as in Fig. 3, did not show colocalization of the tumor mass and fat signals.

MSOT images demonstrated different patterns compared with the appearance of the tumors on ultrasonography. The dense vascular patterns observed, indicating malignancy (42, 44), could play a role in tumor characterization within the BI-RADS classification or for cartography of intratumoral heterogeneity leading to improved biopsy guidance. This

possibility was exemplified in Figs. 3L and 6N, whereby ultrasound identified a large mass containing fibroadenoma and malignant tumor, whereby MSOT detected the highly vascular malignant lesion. In a second example, Fig. 3C and F depict markedly different tumor appearance between MSOT and ultrasound images, with MSOT exhibiting a highly heterogeneous pattern extending well beyond the lesion seen by ultrasonography. Such complementary contrast between MSOT and ultrasonography may change the views on tumor mass extent and biopsy guidance.

MSOT may be further clinically useful for identifying tumor skin infiltration. Disruptions of the melanin layer and skin vascularization, seen on Fig. 4, could guide surgery and overall therapy planning when skin infiltration is suspected. MSOT could help avoiding punch biopsies, especially as current mammographic imaging cannot distinguish between cutaneous edema (e.g., due to lymph node metastasis) and tumor skin infiltration. Furthermore, the extent of the tumor to subcutaneous layers is valuable in planning subcutaneous mastectomy.

Compared with DOI of breast cancer (10–19, 45–49), the MSOT patterns were found showcasing the merits of the superior optoacoustic resolution. DOI cannot observe vascularization patterns, due to the strong photon scattering in tissue and the low resolution achieved. In contrast to optoacoustic methods that resolve breast tumors with 200–300 μm resolution, DOI methods offer a resolution of 2–3 mm or lower. Therefore, only a bulk value per tumor mass can be typically recorded. Moreover, photon diffusion leads to an imaging problem that is highly ill-posed, a feature which significantly reduces the quantification accuracy over high-resolution methods and may lead to strong image artifacts. Therefore, DOI has not been shown suitable to observe the morphologic tumor characteristics observed by MSOT.

The MSOT system described here offers novel features compared with previous optoacoustic studies employing at most 2 wavelengths (25, 36). Advanced illumination and detection technology enabled MSOT at 28 wavelengths at approximately 2-Hz scan times. The use of a large number of wavelengths improves the accuracy of spectral unmixing over systems using 2 wavelengths (41) and enabled unmixing of four spectral components. In addition, fast scanning technology minimizes motion artifacts, which allows seamless coregistration of images collected at different wavelengths and improves the accuracy of spectral unmixing. The MSOT implementation herein also employed curved arrays for improving resolution and overall image quality (32) over linear ultrasound element-arrays or fixed scan geometries that yield lower resolution (25). Conversely, handheld systems are more sensitive to motion over fixed geometries. Moreover, access to deep seated tumors may require adjustment of the handheld scanner to obtain a preferable angle of access, in analogy to practices common in handheld ultrasonography.

Despite the recent technical advances described in the previous paragraph, handheld MSOT can be substantially improved. One advance would be to integrate US into the handheld device, to allow truly multimodal imaging allowing for accurate image registration between the two modalities, in analogy to implementations developed in small-animal imaging (50). Another improvement would be to reduce the effects of wavelength- and depth-dependent fluence attenuation on the optoacoustic images (36). This would be particularly important for accurately calculating oxygen saturation (SO_2) maps, especially as it has been shown that SO_2 images based on linear unmixing become inaccurate with increasing depth (36). It may also be useful to include absorption of melanin in MSOT unmixing, to improve imaging of skin oxygenation.

Overall, MSOT allowed individualized label-free readings of vascularization/angiogenesis patterns in high-resolution, enabling understanding of parameters not only on a per tumor level but even within the intratumoral environment, revealing variations in the tumor spatial heterogeneity among tumors. High peripheral TBV values and weak intratumoral TBV contributions were preliminarily shown to differentiate tumors from adjacent nonmalignant tissues in a broad range of tumor sizes; nevertheless achieving highest TBV contrast in smaller tumors. Understanding this spatial tumor heterogeneity may provide valuable insights into breast cancer pathogenesis, progression, and response to treatment. Some tumors exhibited strong Hb signals, indicative of tumor hypoxia. In the future, careful analysis of Hb and inferred tissue hypoxia may be useful in assessing functional aspects of tumors. Moreover, HbO_2 flare has been suggested as an early predictor of neoadjuvant chemotherapy (46). High-resolution HbO_2 imaging afforded by MSOT may lead to more precise localization of these signals in relation to the tumors, possibly improving the overall accuracy of the observation. In the future, we expect improvements in the quantification of spectral components, especially in regard to correcting for the effects of depth- and wavelength-dependent fluence effects on the data collected (36) and relation of the patterns observed to diagnostic and theranostic applications.

Disclosure of Potential Conflicts of Interest

V. Ntziachristos holds ownership interest (including patents) in iThera Medical GmbH. No potential conflicts of interest were disclosed by the other authors.

Authors' Contributions

Conception and design: S. Metz, R. Meier, E.J. Rummeny, V. Ntziachristos
Development of methodology: G. Diot, V. Ntziachristos
Acquisition of data (provided animals, acquired and managed patients, provided facilities, etc.): G. Diot, S. Metz, A. Noske, R. Meier, E. Rummeny
Analysis and interpretation of data (e.g., statistical analysis, biostatistics, computational analysis): G. Diot, S. Metz, A. Noske, E. Liapis, S.V. Ovsepian, R. Meier
Writing, review, and/or revision of the manuscript: G. Diot, S. Metz, A. Noske, B. Schroeder, S.V. Ovsepian, R. Meier, E. Rummeny, V. Ntziachristos
Administrative, technical, or material support (i.e., reporting or organizing data, constructing databases): G. Diot, S. Metz, A. Noske, R. Meier
Study supervision: G. Diot, E. Rummeny, V. Ntziachristos

Grant Support

The research leading to these results has received funding from the Deutsche Forschungsgemeinschaft (DFG), Sonderforschungsbereich-824 (SFB-824), subproject A1, and Gottfried Wilhelm Leibniz Prize 2013 (NT 3/10-1).

The costs of publication of this article were defrayed in part by the payment of page charges. This article must therefore be hereby marked *advertisement* in accordance with 18 U.S.C. Section 1734 solely to indicate this fact.

Received December 20, 2016; revised March 7, 2017; accepted August 31, 2017; published OnlineFirst September 12, 2017.

References

1. Torre LA, Bray F, Siegel RL, Ferlay J, Lortet-Tieulent J, Jemal A. Global cancer statistics, 2012. CA Cancer J Clin 2015;65:87–108.
2. Cardoso F, Harbeck N, Fallowfield L, Kyriakides S, Senkus E, on behalf of the EGW Group. Locally recurrent or metastatic breast cancer: ESMO Clinical Practice Guidelines for diagnosis, treatment and follow-up. Ann Oncol 2012;23:vii11–vii19.
3. Sickles EA. Breast imaging: from 1965 to the present. Radiology 2000; 215:1–16.
4. Saslow D, Boetes C, Burke W, Harms S, Leach MO, Lehman CD, et al. American cancer society guidelines for breast screening with MRI as an adjunct to mammography. CA Cancer J Clin 2007;57:75–89.
5. Kriege M, Brekelmans CTM, Boetes C, Besnard PE, Zonderland HM, Obdeijn IM, et al. Efficacy of MRI and mammography for breast-cancer screening in women with a familial or genetic predisposition. N Engl J Med 2004;351:427–37.
6. Turnbull L, Brown S, Harvey I, Olivier C, Drew P, Napp V, et al. Comparative effectiveness of MRI in breast cancer (COMICE) trial: a randomised controlled trial. Lancet 375:563–71.
7. Teh W, Wilson ARM. The role of ultrasound in breast cancer screening. A consensus statement by the European Group for breast cancer screening. Eur J Cancer 1998;34:449–50.
8. Berg WA, Gutierrez L, NessAiver MS, Carter WB, Bhargavan M, Lewis RS, et al. Diagnostic accuracy of mammography, clinical examination, US, and MR imaging in preoperative assessment of breast cancer. Radiology 2004;233:830–49.
9. Ntziachristos V, Yodh AG, Schnall M, Chance B. Concurrent MRI and diffuse optical tomography of breast after indocyanine green enhancement. Proc Natl Acad Sci 2000;97:2767–72.
10. Grosenick D, Rinneberg H, Cubeddu R, Taroni P. Review of optical breast imaging and spectroscopy. J Biomed Opt 2016;21:91311.
11. Fang Q, Selb J, Carp S a S, Boverman G, Miller EL, Brooks DH, et al. Combined optical and X-ray tomosynthesis breast imaging. Radiology 2011;258:89–97.
12. Brown JQ, Wilke LG, Geradts J, Kennedy SA, Palmer GM, Ramanujam N. Quantitative optical spectroscopy: a robust tool for direct measurement of breast cancer vascular oxygenation and total hemoglobin content in vivo. Cancer Res 2009;69:2919–26.
13. Tromberg BJ, Pogue BW, Paulsen KD, Yodh AG, Boas DA, Cerussi AE. Assessing the future of diffuse optical imaging technologies for breast cancer management. Med Phys 2008;35:2443–51.
14. Leproux A, Kim YM, Min JW, McLaren CE, Chen W-P, O'Sullivan TD, et al. Differential diagnosis of breast masses in South Korean premenopausal women using diffuse optical spectroscopic imaging. J Biomed Opt 2016;21:74001.
15. Wang J, Jiang S, Li Z, diFlorio-Alexander RM, Barth RJ, Kaufman PA, et al. In vivo quantitative imaging of normal and cancerous breast tissue using broadband diffuse optical tomography. Med Phys 2010; 37:3715–24.
16. Jiang S, Pogue BW, Carpenter CM, Poplack SP, Wells WA, Kogel CA, et al. Evaluation of breast tumor response to neoadjuvant chemotherapy with tomographic diffuse optical spectroscopy: case studies of tumor region-of-interest changes. Radiology 2009;252:551–60.
17. Tromberg BJ, Zhang Z, Leproux A, O'Sullivan TD, Cerussi AE, Carpenter PM, et al. Predicting responses to neoadjuvant chemotherapy in breast cancer: ACRIN 6691 trial of diffuse optical spectroscopic imaging. Cancer Res 2016;76:5933–44.
18. Choe R, Corlu A, Lee K, Durduran T, Konecky SD, Grosicka-Koptyra M, et al. Diffuse optical tomography of breast cancer during neoadjuvant chemotherapy: a case study with comparison to MRI. Med Phys 2005; 32:1128–39.
19. Pakalniskis M, Wells W. Tumor angiogenisis change estimated by using diffuse optical spectroscopic tomography: demonstrated correlation in women undergoing neoadjuvant chemotherapy for invasive breast cancer? Radiology 2011;259:365–74.
20. Taruttis A, Ntziachristos V. Advances in real-time multispectral optoacoustic imaging and its applications. Nat Phot 2015;9:219–27.
21. Ntziachristos V. Going deeper than microscopy: the optical imaging frontier in biology. Nat Meth 2010;7:603–14.
22. Wang L V, Yao J. A practical guide to photoacoustic tomography in the life sciences. Nat Meth 2016;13:627–38.
23. Ermilov SA, Fronheiser MP, Nadvoretsky V, Brecht H-P, Su R, Conjusteau A, et al. Real-time optoacoustic imaging of breast cancer using an interleaved two laser imaging system coregistered with ultrasound. Proc. SPIE 7564, Photons Plus Ultrasound: Imaging and Sensing 2010, 75641W (24 February 2010); doi: 10.1117/12.847946; http://dx.doi.org/10.1117/12.847946
24. Kruger RA, Kuzmiak CM, Lam RB, Reinecke DR, Del Rio SP, Steed D. Dedicated 3D photoacoustic breast imaging. Med Phys 2013;40:113301.
25. Heijblom M, Piras D, van den Engh FM, van der Schaaf M, Klaase JM, Steenbergen W, et al. The state of the art in breast imaging using the Twente Photoacoustic Mammoscope: results from 31 measurements on malignancies. Eur Radiol 2016;1–14.
26. Menke J. Photoacoustic breast tomography prototypes with reported human applications. Eur Radiol 2015;25:2205–13.
27. Heijblom M, Piras D, Brinkhuis M, van Hespen JCG, van den Engh FM, van der Schaaf M, et al. Photoacoustic image patterns of breast carcinoma and comparisons with Magnetic Resonance Imaging and vascular stained histopathology. Sci Rep 2015;5:11778.
28. Fukutani K, Someda Y, Taku M, Asao Y, Kobayashi S, Yagi T, et al. Characterization of photoacoustic tomography system with dual illumination. 2011; 78992J–7.
29. Ermilov SA, Fronheiser MP, Brecht H-P, Su R, Conjusteau A, Mehta K, et al. Development of laser optoacoustic and ultrasonic imaging system for breast cancer utilizing handheld array probes. International Society for Optics and Photonics; 2009: 717703–10.
30. Kruger RA, Lam RB, Reinecke DR, Del Rio SP, Doyle RP. Photoacoustic angiography of the breast. Med Phys 2010;37:6096–100.
31. Oraevsky AA, Savateeva E V, Solomatin S V, Karabutov AA, Gatalica Z, Khamapirad T. Diagnostic imaging of breast cancer microvasculature with optoacoustic tomography [abstract]. In: Proceedings of the 24th Annual Conference and the Annual Fall Meeting of the Biomedical Engineering Society; 2002 Oct 23–26; Houston, TX. New York (NY): IEEE; 2002.
32. Ermilov S, Stein A, Conjusteau A, Gharieb R, Lacewell R, Miller T, et al. Detection and noninvasive diagnostics of breast cancer with 2-color laser optoacoustic imaging system. Photons Plus Ultrasound: Imaging and Sensing 2007, 6437, 43703–43703.
33. Neuschmelting V, Burton NC, Lockau H, Urich A, Harmsen S, Ntziachristos V, et al. Performance of a multispectral optoacoustic tomography (MSOT) system equipped with 2D vs. 3D handheld probes for potential clinical translation. Photoacoustics 2016;4:1–10.
34. Buehler A, Kacprowicz M, Taruttis A, Ntziachristos V. Real-time handheld multispectral optoacoustic imaging. Opt Lett 2013;38:1404–6.
35. Taruttis A, van Dam GM, Ntziachristos V. Mesoscopic and macroscopic optoacoustic imaging of cancer. Cancer Res 2015;75:1548–59.
36. Tzoumas S, Nunes A, Olefir I, Stangl S, Symvoulidis P, Glasl S, et al. Eigenspectra optoacoustic tomography achieves quantitative blood oxygenation imaging deep in tissues. Nat Commun 2016;7: 12121.
37. D'Orsi CJ, Sickles EA, Mendelson EB, Morris EA. ACR BI-RADS® Atlas, Breast Imaging Reporting and Data System. Reston, VA: American College of Radiology; 2013.
38. Rosenthal A, Razansky D, Ntziachristos V. Fast semi-analytical model-based acoustic inversion for quantitative optoacoustic tomography. IEEE Trans Med Imaging 2010;29:1275–85.
39. Prahl S. Tabulated molar extinction coefficient for hemoglobin in water. Oregon Med Laser Cent 1998;4. Available at: http://omlc.org/spectra/index.html
40. Holash J, Maisonpierre PC, Compton D, Boland P, Alexander CR, Zagzag D, et al. Vessel cooption, regression, and growth in tumors mediated by angiopoietins and VEGF. Science 1999;284:1994–8.
41. Yancopoulos GD, Davis S, Gale NW, Rudge JS, Wiegand SJ, Holash J. Vascular-specific growth factors and blood vessel formation. Nature 2000;407:242–8.
42. Hanahan D, Weinberg RA. Hallmarks of cancer: the next generation. Cell 144:646–74.
43. Gatenby RA, Gillies RJ. Why do cancers have high aerobic glycolysis? Nat Rev Cancer 2004;4:891–9.
44. Nishida N, Yano H, Nishida T, Kamura T, Kojiro M. Angiogenesis in cancer. Vasc Health Risk Manag 2006;2:213–9.

45. Ueda S, Roblyer D, Cerussi A, Durkin A, Leproux A, Santoro Y, et al. Baseline tumor oxygen saturation correlates with a pathologic complete response in breast cancer patients undergoing neoadjuvant chemotherapy. Cancer Res 2012;72:4318–28.
46. Roblyer D, Ueda S, Cerussi A, Tanamai W, Durkin A, Mehta R, et al. Optical imaging of breast cancer oxyhemoglobin flare correlates with neoadjuvant chemotherapy response one day after starting treatment. Proc Natl Acad Sci 2011;108:14626–31.
47. Cerussi A, Hsiang D, Shah N, Mehta R, Durkin A, Butler J, et al. Predicting response to breast cancer neoadjuvant chemotherapy using diffuse optical spectroscopy. Proc Natl Acad Sci U S A 2007;104:4014–9.
48. Jiang S, Pogue BW, Kaufman PA, Gui J, Jermyn M, Frazee TE, et al. Predicting breast tumor response to neoadjuvant chemotherapy with diffuse optical spectroscopic tomography prior to treatment. Clin Cancer Res 2014; 20:6006–15.
49. Jiang S, Pogue BW. A comparison of near-infrared diffuse optical imaging and 18F-FDG PET/CT for the early prediction of breast cancer response to neoadjuvant chemotherapy. J Nucl Med 2016;57: 1166–7.
50. Olefir I, Merčep E, Burton NC, Ovsepian S V, Ntziachristos V. Hybrid multispectral optoacoustic and ultrasound tomography for morphological and physiological brain imaging. J Biomed Opt 2016;21:86005.